Nanoscale

PAPER

View Article Online
View Journal | View Issue

Cite this: *Nanoscale*, 2025, **17**, 19828

Temperature-dependent sign reversal of tunneling magnetoresistance in van der Waals ferromagnetic heterojunctions

Qiaoqiao Wang, †[a] Jiarui Liu,†[a] Chao Yang,[a] Hanzhang Zhao,[a] Yongyi Wu, [a] Feiyan Hou,[a] Tao Li*[a] and Tai Min*[a,b,c]

Received 3rd May 2025,
Accepted 22nd July 2025

DOI: 10.1039/d5nr01813g

rsc.li/nanoscale

Magnetic tunnel junctions (MTJs) are the elemental devices for advanced spintronic technologies, where tunneling magnetoresistance (TMR) serves as one of the key performance metrics. Here, we used the topologically nontrivial magnetic insulator $CrVI_6$ and magnetic metal Fe_3GeTe_2 to fabricate $CrVI_6/Fe_3GeTe_2$ heterojunctions and $Fe_3GeTe_2/CrVI_6/Fe_3GeTe_2$ MTJs. In the heterojunctions, the addition of $CrVI_6$ led to a 180% coercive field enhancement of Fe_3GeTe_2 near the Curie temperature (T_C) of $CrVI_6$, which originated from the antiferromagnetic coupling between them. More importantly, a temperature-dependent TMR sign reversal in the $Fe_3GeTe_2/CrVI_6/Fe_3GeTe_2$ MTJ was observed, gradually transforming from a negative value at low temperature to a positive value above 60 K, close to the T_C of $CrVI_6$. The results demonstrate that the spin-filtering effect with polarity opposite to Fe_3GeTe_2 in $CrVI_6$ constitutes the primary mechanism for temperature-dependent TMR sign reversal. Furthermore, under combined temperature and bias voltage modulation, we observed the coexistence of both positive and negative TMR. This finding suggests the potential extension of conventional bistate MTJ operation to multi-state functionality. This research broadens the controllable degrees of freedom in MTJs and advances van der Waals magnet-based spintronic devices.

Introduction

Magnetic tunnel junctions (MTJs) are the fundamental building blocks of various spintronic devices,[1] which have demonstrated extensive and pivotal applications across a plethora of cutting-edge fields, including magnetic random-access memories, magnetic sensors, spin logics, and neuromorphic computing devices.[2–5] Tunneling magnetoresistance (TMR) is one of the core properties used to evaluate the functionality of MTJs.[6] TMR is defined as $(R_{AP} - R_P)/R_P$, where R_{AP} and R_P represent the tunneling resistances for antiparallel and parallel magnetization alignments of the ferromagnetic electrodes, respectively. The sign of TMR can be reversed upon alterations in external conditions such as bias voltage[7–11] and temperature.[12–14] Given that this sign-reversal effect can significantly expand the controllable parameter space within MTJs, it has attracted widespread attention and in-depth research in recent years. In particular, a real-time programmable logic gate device has been constructed using MTJs featuring voltage-controllable and sign-reversible TMR effects,[15] which has strengthened the importance of the sign-reversal TMR effect. Notably, with the continuous emergence of two-dimensional van der Waals (vdW) magnetic materials in recent years,[16,17] MTJs constructed completely from vdW materials have been widely studied.[18–20] In particular, some bias-dependent sign reversal of TMR in vdW MTJs has been observed and attributed to the significant contribution of the spin-resolved density of states in the metallic ferromagnet.[21–23] However, the temperature-dependent sign reversal of TMR has not yet been reported in vdW MTJ systems, whose performance strongly depends on the tunneling barrier used in the MTJ.[24,25] $CrVI_6$ (CVI) has been theoretically predicted to be a topological ferromagnetic insulator[26] and has been experimentally observed to exhibit the topological Kerr effect as well as excellent magnetic characteristics.[27,28] Using this topologically nontrivial magnetic insulator as the tunneling barrier in vdW MTJs may offer unusual tunneling behavior, and its effect on the TMR sign reversal also remains unclear.

---

[a] *Center for Spintronics and Quantum Systems, State Key Laboratory for Mechanical Behavior of Materials, School of Materials Science and Engineering, Xi'an Jiaotong University, Xi'an, Shaanxi 710049, China. E-mail: taoli66@xjtu.edu.cn, tai.min@nju.edu.cn*

[b] *Solid State Microstructure National Key Lab and Collaborative Innovation Centre of Advanced Microstructures, Nanjing University, Nanjing 210093, China*

[c] *School of Materials Science and Intelligent Engineering, Nanjing University, Suzhou 215163, China*

† These authors contributed equally to this work, and they should be viewed as first authors.

In this work, we used the topologically nontrivial ferromagnetic insulator CVI and the ferromagnetic metal Fe_3GeTe_2 (FGT) to fabricate CVI/FGT heterojunctions and FGT/CVI/FGT MTJs. In the CVI/FGT heterojunctions, the addition of CVI enhanced the coercive field (H_C) of FGT by approximately 180% at 60 K, close to the Curie temperature (T_C) of CVI. We attribute this phenomenon to antiferromagnetic (AFM) coupling between CVI and FGT, based on systematic exclusion of prevalent mechanisms known to change H_C in ferromagnetic heterostructures (spin pinning and charge transfer), combined with direct experimental evidence of AFM coupling obtained through low-temperature magneto-optical Kerr effect (MOKE) measurements. In the FGT/CVI/FGT MTJs, a temperature-dependent sign reversal of TMR was observed. The TMR gradually decreased from a maximum value of −13% at 2 K and reversed to a positive value at approximately 60 K. The sign reversal temperature is also close to the T_C of CVI. We speculate that the negative TMR arises from the opposite polarity of the CVI spin filter and FGT electrodes, where the spin-polarized barrier in CVI suppresses (enhances) carrier transport in FGT when the CVI and FGT magnetizations are aligned parallel (antiparallel). Furthermore, we observed bias-dependent TMR sign reversal, as well as the coexistence of both positive and negative TMR signals under combined bias voltage and temperature modulation. These findings enrich the understanding of vdW magnetic device performance by the coupling effect at the magnetic interface and offer a new candidate for next-generation spintronic devices.

Results and discussion

CVI/FGT heterojunctions and the FGT/CVI/FGT MTJs were fabricated *via* a dry-transfer method using mechanically exfoliated CVI and FGT flakes. The magnetic properties of the CVI (28.7 nm)/FGT (21 nm) heterojunction were investigated using standard Hall measurements (Fig. 1a). For comparison, we also fabricated pure FGT devices of identical thickness to examine the effect of CVI on the magnetic properties of FGT. Optical microscopy images of both the CVI/FGT heterojunction and pure FGT are provided in Fig. S2 in the SI. Different from the metallic characteristics of FGT, CVI exhibits high resistance (minimum 400 kΩ at 30 K) and near-insulating characteristics (see Fig. S4), more than two orders of magnitude higher than that of FGT (0.5 kΩ at 30 K). Consequently, in the CVI/FGT heterojunction, current predominantly flows through FGT, and the Hall voltage originates from the FGT layer only, while CVI plays a role in modulating the magnetic properties of FGT. Temperature-dependent R_{xx} values of the CVI/FGT heterojunction (Fig. 1b) and those of pure FGT (see Fig. S5a) demonstrate metallic behavior at high temperatures (20–300 K) and undergo a metal–insulator transition at 20 K, consistent with prior reports on FGT. This suggests a transition from phonon-scattering-dominated conduction at high temperatures to a hopping conduction mechanism at low temperatures.[29] Additionally, a distinct kink was observed near 150 K in both the CVI/FGT heterojunction and pure FGT, which is expected to correspond to the T_C of FGT.[30] The temperature-dependent

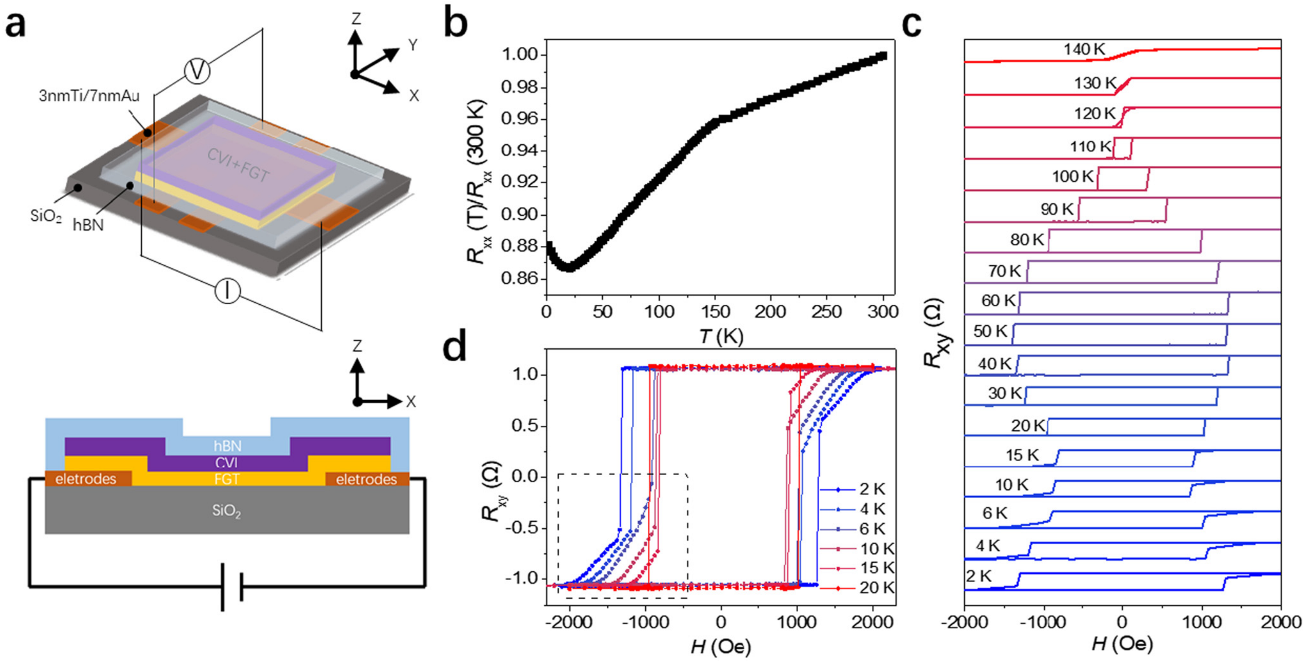

Fig. 1 Transport and Hall measurements of the CVI/FGT heterojunction. (a) Schematic diagram of the CVI (top)/FGT (bottom) heterojunction for Hall measurements. (b) Temperature-dependent R_{xx} curve of the CVI/FGT heterojunction. (c) Temperature-dependent anomalous Hall resistance hysteresis loops of the CVI/FGT heterojunction. (d) Temperature-dependent anomalous Hall resistance hysteresis loops of the CVI/FGT heterojunction at $T \leq 20$ K. The section enclosed by the black dotted square shows a gradual magnetization switching process close to the saturation field.

anomalous Hall resistance hysteresis loops for the CVI/FGT heterojunction (Fig. 1c) and pure FGT (see Fig. S5b) exhibit a non-monotonic temperature dependence of H_C. Different from the square shape of the hysteresis loop, below the metal–insulator transition temperature, the hysteresis loops show a gradual increase toward saturation fields (enclosed by a black dashed square, Fig. 1d and S5c in the SI), indicative of multidomain formation in FGT during the switching process.[31]

Temperature-dependent H_C curves of the CVI/FGT heterojunction and pure FGT (Fig. 2a) were extracted from anomalous Hall resistance hysteresis loops. Both curves show similar trends, but the heterojunction exhibits significantly enhanced H_C in the temperature range between 15 K and 90 K. Notably, at 50 K, the H_C increases by 70%, from 802 Oe (pure FGT) to 1349 Oe (CVI/FGT). This finding is verified by another CVI (23.1 nm)/FGT (18 nm) heterojunction, which exhibits a maximum 180% enhancement of H_C at 60 K (see Fig. S6). To further elucidate the enhancement mechanism of CVI on the H_C of FGT, the temperature-dependent H_C curves were divided into three regions for analysis (Fig. 2a). In region I ($T > 90$ K), the H_C values of the CVI/FGT heterojunction and pure FGT exhibit consistency, which aligns with prior observations in other vdW ferromagnetic heterojunctions.[30,32] This temperature is above the T_C of CVI, which only functions as a non-magnetic insulator, with negligible impact on the magnetic characteristics of FGT. In region II ($15\text{ K} < T < 90$ K), the H_C values of the CVI/FGT heterojunction exhibit a pronounced enhancement compared to pure FGT. The maximum H_C enhancement occurs at 50 K, close to the T_C of the CVI crystal (~55 K),[28] which preliminarily indicates that the ferromagnetism of CVI plays a pivotal role in modulating the H_C of FGT. In region III ($T < 15$ K), the nearly overlapping curves of the CVI/FGT heterojunction and pure FGT are observed, which suggests a weakened influence of CVI on the magnetism of FGT. This may arise from the emergence of a multidomain structure in FGT at low temperatures (Fig. 1d), which weakens its interlayer coupling with CVI.

To further investigate the mechanism underlying the enhancement of the H_C in FGT mediated by CVI during region II, analysis was performed on two prevalent mechanisms for H_C modulation in two-dimensional ferromagnetic heterostructures: spin pinning and charge transfer.[30,32] The spin pinning mechanism was eliminated from consideration because pure CVI exhibits lower H_C compared to pure FGT in the 30–50 K temperature range,[28] rendering it incapable of enhancing the H_C of FGT through this effect, directly contradicting the experimental observations. Regarding charge transfer, prior work calculated that electron transfer from FGT to $Cr_2Ge_2Te_6$ reduces the magnetic anisotropy energy of FGT, consequently diminishing the corresponding H_C.[32] Parallel calculations for the interface between FGT and CVI (see Fig. S7) revealed similar charge transfer from FGT to CVI, which would likewise decrease the H_C of FGT, again opposing the experimental findings. Furthermore, experimental observations indicate that charge-transfer-induced modulation of coercive fields are confined to interfacial contact regions.[32] To test this, we

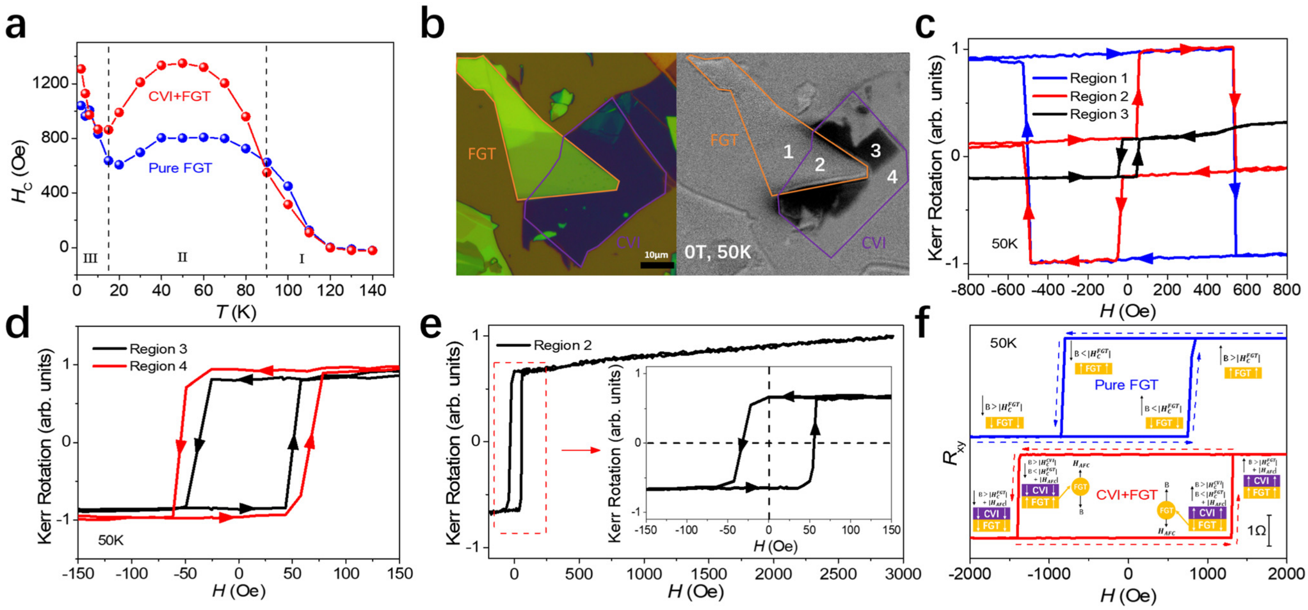

Fig. 2 Significant enhancement of H_C *via* antiferromagnetic coupling in the CVI/FGT heterojunction. (a) Temperature-dependent H_C curves of the CVI/FGT heterojunction and pure FGT. (b) Optical microscopy image of the CVI/FGT heterojunction (left) and the magnetic domain structure of the CVI/FGT heterojunction after zero-field cooling to 50 K (right). (c) Hysteresis loops of the MOKE for regions 1–3 at 50 K. (d) Hysteresis loop comparison of the MOKE between region 3 and region 4 at 50 K. (e) Hysteresis loop of the MOKE for region 2 at 50 K with a ±200 Oe field, after magnetization using a 3000 Oe field. (f) Anomalous Hall resistance hysteresis loops of the pure FGT and the CVI/FGT heterojunction at 50 K, with corresponding schematics of the magnetization in each layer. In the diagram, B, H_C^{CVI}, H_C^{FGT} and H_{AFC} represent the external magnetic field, H_C of CVI, H_C of FGT, and effective magnetic field from the AFM coupling effect, respectively.

fabricated a partially CVI (28 nm)-covered FGT (19 nm) heterojunction device and measured its temperature-dependent H_C. As shown in Fig. S8 in the SI, both CVI-covered and bare FGT regions exhibit identical H_C behavior. This demonstrates that modulation of H_C in FGT by CVI occurs uniformly across the entire magnetic domain rather than being confined to the contact interface, further excluding the charge transfer mechanism. Consequently, the charge transfer mechanism was conclusively excluded.

Subsequently, to directly investigate the interaction mechanism between CVI and FGT, we fabricated a partially CVI (11.2 nm)-covered FGT (30 nm) heterojunction and conducted low-temperature MOKE measurements, with the optical microscopy image of the heterostructure presented on the left side of Fig. 2b. The right side of Fig. 2b displays the magnetic domain imaging results obtained after zero-field cooling from room temperature to 50 K, where four distinct regions are identified: region 1 represents the non-contacted part of the FGT single domain covered by CVI, region 2 represents the directly contacted part between the CVI single domain and the FGT single domain, region 3 represents the non-contacted part of the CVI single domain that covers FGT, and region 4 represents the CVI single domain that does not cover FGT.

It can be observed that the CVI single domain that covers FGT (region 2 and region 3) spontaneously developed magnetic contrast opposite to both the FGT single domain covered by CVI (region 1 and region 2) and the CVI single domain that does not cover FGT (region 4) in the absence of an applied magnetic field. Region 2 exhibited magnetic contrast more similar to region 1 due to the stronger magnetization signal of FGT at 50 K, which overrode the CVI contribution. This domain configuration provides two crucial insights: first, the interaction between FGT and CVI exists beyond the contact part, which again rules out the charge transfer mechanism; second, the opposite magnetic domain contrast spontaneously formed by the contact between FGT and CVI observed under a zero magnetic field preliminarily proves the existence of antiferromagnetic coupling between them.

Subsequently, hysteresis loop measurements using the MOKE on regions 1–4 at 50 K were performed. Fig. 2c displays the results for regions 1–3, revealing two key findings: first, at 50 K, CVI exhibits smaller H_C than that of FGT, verifying the process for exclusion of the spin pinning effect in the previous discussion; second, region 2 (FGT + CVI) shows two independent square hysteresis loops, whose H_C values match those of region 1 (FGT) and region 3 (CVI), respectively. The presence of two independent square loops in region 2 further rules out the spin-pinning mechanism, while the identical coercive fields between the contact and non-contact regions again exclude the charge transfer mechanism. Fig. 2d compares the hysteresis loops of regions 3 and 4, demonstrating that the CVI single domain that covers FGT (region 3) has reduced H_C compared to the CVI single domain that does not cover FGT (region 4). Therefore, at 50 K, CVI with a smaller H_C than that of FGT causes an increase in the H_C of FGT while reducing its own H_C. This, in the case of excluding charge transfer, further implies the existence of antiferromagnetic coupling between the two. Specifically, we applied a 3000 Oe field to saturate magnetization of FGT in the positive direction, then measured the hysteresis loop of region 2 (FGT + CVI) under a 200 Oe field (Fig. 2e). With magnetization of FGT fixed, only the hysteresis loop of CVI was observed, which exhibits a distinct positive exchange bias field (a positive exchange bias field of 13 Oe exists at a coercive field of 30 Oe). This indicates that after fixing the positive-direction magnetization of FGT, CVI more readily forms a negative-direction magnetic moment, while forming a positive-direction magnetic moment is more difficult, suggesting that CVI and FGT tend to form an antiferromagnetic arrangement. This further confirms the antiferromagnetic coupling between CVI and FGT.

Finally, the enhancement effect of antiferromagnetic coupling in the CVI/FGT heterojunction on the H_C of FGT was demonstrated in detail using a model. Fig. 2f presents the anomalous Hall resistance hysteresis loops for both the CVI/FGT heterojunction and pure FGT at 50 K, with corresponding schematics of the magnetization in each layer. For pure FGT, when the external magnetic field gradually sweeps from the negative saturation to the positive saturation along the blue dotted line, the magnetic moment reverses only when the external magnetic field is greater than the H_C of FGT. For the CVI/FGT heterojunction, since the H_C of CVI is smaller than that of FGT at 50 K, as the magnetic field gradually increases from negative to positive along the red dotted line, the magnetic moment of CVI switches first. Meanwhile, the antiferromagnetic coupling reduces the H_C of CVI. The magnetic moments of CVI and FGT switch from a parallel to an antiparallel alignment. Then, due to AFM coupling between FGT and CVI, FGT is influenced by both the external magnetic field and the AFM coupling effect from CVI, which is antiparallel to the external field direction. The magnetic moment of the FGT layer can only be reversed when the external magnetic field overcomes the additional AFM coupling energy from CVI. This leads to the H_C enhancement in the CVI/FGT heterojunction in region II of Fig. 2a. In conclusion, the combined experimental and modeling analyses demonstrate that the enhancement of the H_C in FGT induced by CVI originates from antiferromagnetic coupling between the two materials. Moreover, it can be found that, in region II, the enhancement effect of CVI on the coercivity of FGT gradually weakens as the temperature decreases further. This behavior likely originates from temperature-dependent transitions in interlayer magnetic coupling states, a phenomenon previously documented in multilayer systems.[33,34] For example, in GaMnAsP-based trilayer structures, a transition from antiferromagnetic coupling to ferromagnetic coupling has been observed as the temperature drops.[33]

Beyond the FGT/CVI heterojunctions, we also investigated the tunneling properties of the FGT (36 nm)/CVI (2.8 nm)/FGT (5 nm) MTJ using standard two-terminal constant voltage measurements (Fig. 3a). Temperature-dependent tunneling resistance (R_{tunnel}) measurements (Fig. 3b) exhibit an overall increasing trend as the temperature decreases. The tunneling

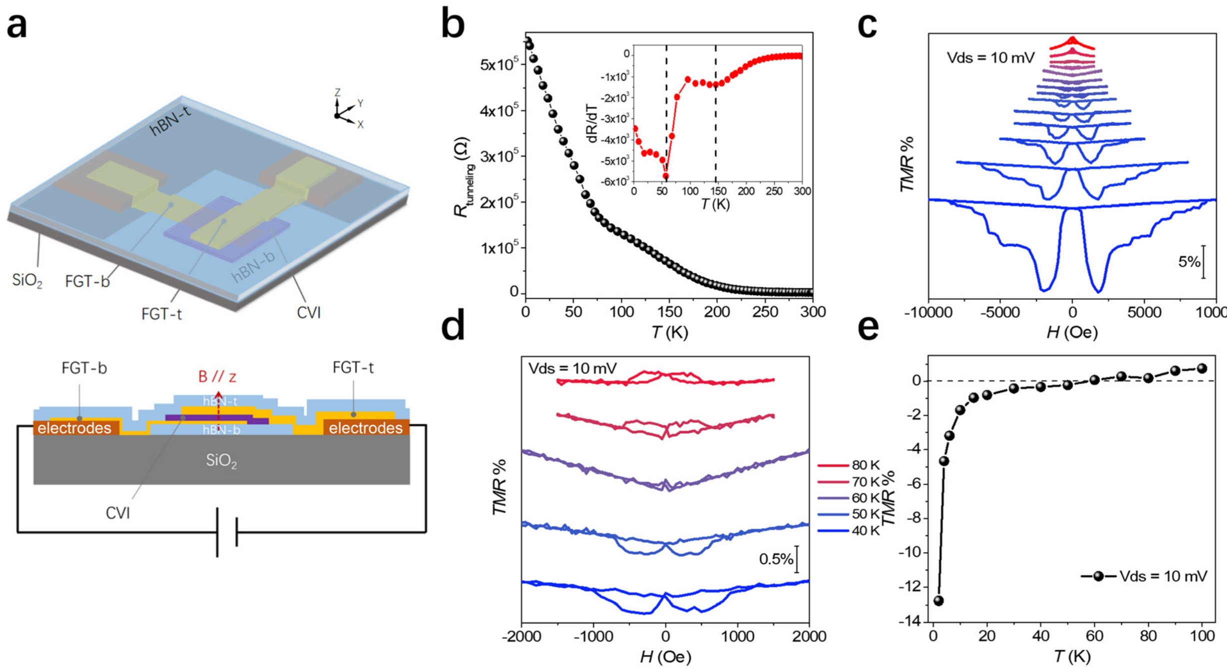

Fig. 3 Temperature-dependent TMR sign reversal of the FGT/CVI/FGT MTJ. (a) Schematic diagram of the FGT/CVI/FGT MTJ and tunneling measurement apparatus. The thick FGT is stacked on top of the CVI, and the thin FGT is below the CVI layer. (b) Temperature-dependent R_{tunnel} curve of the FGT/CVI/FGT MTJ. The inset shows the derivative of the temperature-dependent R_{tunnel} curve, where a minimum is observed near both 60 K and 150 K, labeled by the black dotted line. (c) Temperature-dependent TMR curves of the CVI/FGT/FGT MTJ at a bias voltage of 10 mV. (d) Temperature-dependent TMR curves of the FGT/CVI/FGT MTJ at the temperature range of 40–80 K. (e) Temperature dependence of the TMR peak value in the FGT/CVI/FGT MTJ.

resistance gradient (inset of Fig. 3b) shows two distinct minima near 150 K and 60 K, which correspond to the T_C of FGT and CVI, respectively. Meanwhile, the current–voltage (I–V) curve of the FGT/CVI/FGT MTJ at 2 K (see Fig. S9) also demonstrated a nonlinear tunnelling behavior. The TMR behavior of the FGT/CVI/FGT MTJ was characterized by sweeping an external magnetic field along the out-of-plane direction. Typically, when the ferromagnetic electrodes are arranged in antiparallel (parallel) magnetization, the MTJ exhibits high (low) resistance, yielding positive TMR. This is jointly determined by the energy bands of ferromagnetic materials and the electron tunneling characteristics, which can be described by the Julliere model.[35] Unexpectedly, the temperature-dependent TMR curves of the FGT/CVI/FGT MTJ (Fig. 3c) exhibit negative TMR at low temperatures (2 K–50 K) and positive TMR at high temperatures (60 K–100 K), which demonstrates a temperature-dependent sign reversal of TMR. Fig. 3d displays the temperature-dependent TMR curves of the MTJ between 40 K and 80 K on an expanded scale, where the TMR signal vanishes at 60 K, which is the critical temperature of the sign reversal that is close to the T_C of CVI observed in Fig. 3b and its reported T_C value (~55 K) in the literature.[28] Fig. 3e illustrates the temperature evolution of the TMR peak value in the MTJ. The peak value of TMR reaches −13% at 2 K, comparable to the reported negative TMR values of other vdW MTJ systems,[32,36,37] and then undergoes a sign reversal to +1% as the temperature rises to 100 K, with the temperature of the sign reversal occurring near 60 K. This temperature-dependent TMR behavior provides compelling evidence that the magnetic ordering of CVI dictates the spin transport characteristics in the FGT/CVI/FGT MTJ. Similarly, this finding is verified by another FGT (33 nm)/CVI (1.4 nm)/FGT (18 nm) MTJ, which exhibits a temperature-dependent TMR sign reversal near 60 K, close to the T_C of CVI, with the TMR peak gradually changing from −7% at 4 K to +0.5% at 80 K (see Fig. S10).

To elucidate the role of the magnetism of CVI in the temperature-dependent TMR sign reversal, we systematically analyzed both the switching process of R_{tunnel} and the corresponding magnetization switching sequence of magnetic layers in the FGT/CVI/FGT MTJ. Fig. 4a shows the magnetic field-dependent R_{tunnel} curve of the FGT/CVI/FGT MTJ at 6 K. When the magnetic field sweeps from −0.5 T to 0.5 T (Fig. 4a, the red curve), the R_{tunnel} initially remains constant in a saturated state. Upon reaching H_C1, R_{tunnel} abruptly drops, followed by an increase, forming a valley. Upon reaching H_C2, R_{tunnel} exhibits a slow increase and forms a quasi-plateau. Finally, upon reaching H_C3, the R_{tunnel} increases again and stabilizes into saturation, maintaining a field-independent behavior. Considering the trilayer magnetic structure of the FGT/CVI/FGT MTJ, the H_C1, H_C2, and H_C3 should correspond to the coercive fields of the three magnetic layers. It is worth noting that H_C1 in another FGT/CVI/FGT MTJ appears before field reversal, demonstrating negative coercivity behavior (see Fig. S10f). Given that negative coercive fields are characteristic

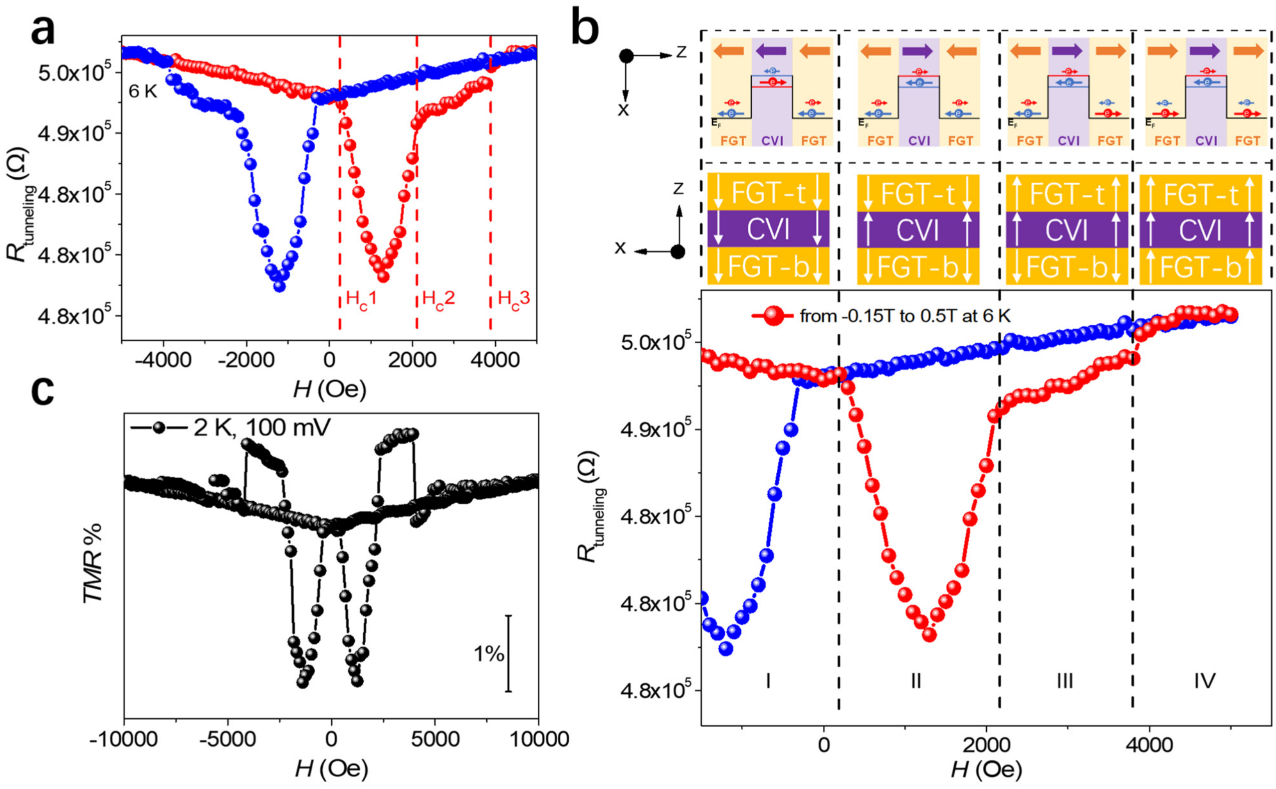

Fig. 4 Magnetization switching sequence and the TMR sign reversal scheme in the FGT/CVI/FGT MTJ. (a) Magnetic field-dependent R_{tunnel} curve of the FGT/CVI/FGT MTJ at 6 K. The red curve represents the process of the magnetic field sweeping from −0.5 T to 0.5 T, and the blue curve represents the reversed sweeping process. The corresponding coercive fields, $H_{\mathrm{C}}1$, $H_{\mathrm{C}}2$, and $H_{\mathrm{C}}3$, are labeled by vertical red dashed lines. (b) The magnetic field-dependent R_{tunnel} curve in the FGT/CVI/FGT MTJ with the magnetic field changing from −0.15 T to 0.5 T at 6 K shows the magnetic configurations of the four stages and their corresponding tunneling mechanism. The red arrow represents spin-up, and the blue arrow represents spin-down, while the size of the arrow represents the majority carriers (large) and minority carriers (small). (c) TMR curve of the CVI/FGT/FGT MTJ at 2 K and 100 mV bias.

of AFM-coupled multilayer systems,[38,39] and no AFM coupling has been reported in FGT/FGT homojunctions,[40,41] the observed negative coercive field in our system provides additional indirect evidence of antiferromagnetic coupling between CVI and FGT. Correspondingly, the magnetization switching sequence in the FGT/CVI/FGT MTJ starts from saturation at −0.5 T. As the field increases, the CVI layer should switch first as it is simultaneously influenced by AFM coupling from both the upper and lower FGT layers, where $H_{\mathrm{C}}1$ corresponds to the coercive field of CVI. As the field continues to increase, considering the thickness-dependent coercivity of FGT,[42] the thick FGT layer switches following CVI, and the thin FGT layer switches the last. Thus, $H_{\mathrm{C}}2$ and $H_{\mathrm{C}}3$ should correspond to the coercive fields of the thick and thin FGT layers, respectively. The blue curve illustrates the switching process of R_{tunnel} as the field sweeps from 0.5 T to −0.5 T, exhibiting a behavior analogous to that of the red curve.

The sign reversal of TMR in the MTJ can be caused by multiple physical mechanisms, such as resonant tunneling,[43] interaction between tunnel electrons and magnetic impurities in the tunnel barrier,[14] asymmetry in electron scattering coefficients between adjacent magnetic layers,[44] bias voltage-induced high-energy localized spin states,[21] interplay between the anisotropic density of states and magnetization reversal,[45] and spin filtering effects.[46] Among these mechanisms, the spin filtering effect is usually employed in the MTJs with magnetic insulating barriers to explain the influence of magnetic insulating layers on the magnitude as well as the sign of TMR.[46–52] Significant spin-filtering effects have been demonstrated experimentally and computationally in vdW systems.[24,25,53,54] We expect that the spin-filtering effect in the CVI layer likely governs the TMR sign reversal in the FGT/CVI/FGT MTJ. Here, we take a section of the magnetic field-dependent R_{tunnel} curve with the magnetic field changing from −0.15 T to 0.5 T at 6 K as an example (Fig. 4b, red curve) to analyze the cause of the occurrence of negative TMR. According to the switching process of the R_{tunnel} accompanying the magnetization switching process, the magnetic field-dependent R_{tunnel} curve can be divided into four stages. Initially, R_{tunnel} exhibits a high resistance state, corresponding to aligned magnetic moments of the three magnetic layers along the −*z* direction under the saturation field (stage I). Then, the R_{tunnel} decreases and exhibits a low resistance state, corresponding to the magnetic moment of the CVI layer switching to the +*z* direction and is arranged antiparallel with the magnetic moments of the upper and lower FGT layers simultaneously (stage II), resulting in a negative TMR. This indicates that the antiparallel alignment of CVI and FGT magnetic moments in FGT/CVI/FGT MTJ corresponds to a larger tunneling probability. The spin filtering effect can enhance tunneling probability at the antiparallel alignment between the magnetic insulating layer and the ferromagnetic electrode by the spin-resolved barrier. The opposite spin polarization between the magnetic insulating layer and the ferromagnetic electrode lowers the barrier for the majority of spins when the magnetic insulating layer and the ferromagnetic electrode are in an antiparallel alignment, increasing tunneling probability. For example, the negative TMR, determined by the opposite polarity of the magnetic insulating layer and the ferromagnetic electrode, has been observed in some systems.[46,52,55] Therefore, in our case, we expect that when the magnetic moments of CVI and FGT are parallel (antiparallel), CVI provides a high (low) tunneling barrier for the majority of spin carriers of FGT. Fig. 4b (top panel) schematically illustrates the corresponding tunneling mechanism for each stage. When the three magnetic layers are aligned parallel to the $-z$ direction (stage I), the majority spin-down carriers tunnel through a relatively high spin-down barrier into the majority spin-down band. The tunneling probability is low and has a high resistance state. When the three magnetic layers are arranged in an anti-parallel manner (stage II), the majority spin-down carriers tunnel through a relatively low spin-down barrier into the majority spin-down band. The tunneling probability increases, and the R_{tunnel} of the device decreases. Then, when the magnetic field is further increased toward 0.5 T, the magnetic moment of the thick FGT layer switches to the $+z$ direction, becoming parallel to the magnetic moment of the CVI layer, while the magnetic moment of the thin FGT layer remains unchanged (stage III). At this time, the majority spin-down carriers tunnel through a relatively low spin-down barrier into the minority spin-down band. The antiparallel configuration between the two FGTs reduces the tunneling probability, resulting in increased resistance. Finally, when the magnetic field reaches saturation along the $+z$ direction, the magnetic moment of the thin FGT layer switches to the $+z$ direction, leading to magnetic moments of three magnetic layers align along the $+z$ direction (stage IV). At this time, the majority spin-up carriers face a high barrier, analogous to stage I, restoring the high-resistance state through an equivalent spin-filtering effect. As a result, the FGT/CVI/FGT MTJ exhibits negative TMR below the T_C of CVI. When the temperature rises above the T_C of CVI, the magnetism of the CVI layer disappears, and it only serves as an ordinary insulating layer. At this time, the device resumes the positive TMR corresponding to the Jullière model.[35] This explains the CVI-mediated TMR sign reversal observed in the FGT/CVI/FGT MTJs. It is worth noting that, in stage III in Fig. 4b, when the tunneling probability reduction induced by an antiparallel FGT alignment outweighs the tunneling probability enhancement from CVI spin filtering, the system can exhibit higher resistance than the initial state, leading to coexisting positive and negative TMR signals. The predicted coexistence of positive and negative TMR signals was experimentally observed in the 2 K, 100 mV TMR curve (Fig. 4(c)), with similar coexistence phenomena detected in the 10 K, 10 mV and 15 K, 10 mV TMR measurements, thereby further validating the accuracy of the constructed model. The coexistence of positive and negative TMR demonstrates that our designed FGT/CVI/FGT MTJ device not only achieves temperature-controlled TMR sign switching but also advances conventional two-state MTJ operation to potential three-state controllability, bearing profound implications for future theoretical and experimental research on MTJs.

Subsequently, to explain the negative TMR, we adopted a modified Jullière model for MTJs with a ferromagnetic insulating spacer layer exhibiting spin-filtering effects. In this framework, the spin polarizations of the two ferromagnetic electrodes are denoted as P_1 and P_3, while the spin-filtering efficiency of the ferromagnetic insulating layer is incorporated into the Jullière model as P_{SF}.[56] In our modeling, we define the parallel state as the configuration where all three magnetic layers are aligned in parallel, while the antiparallel state corresponds to the configuration where the three magnetic layers exhibit mutual antiparallel alignment. It can be obtained as follows:

$$G_{\text{P}} \propto (1+P_1)(1+P_{\text{SF}})(1+P_3)+(1-P_1)(1-P_{\text{SF}})(1-P_3), \quad (1)$$

$$G_{\text{AP}} \propto (1+P_1)(1-P_{\text{SF}})(1+P_3)+(1-P_1)(1+P_{\text{SF}})(1-P_3) \quad (2)$$

Then combining equations:

$$\text{TMR} = \frac{R_{\text{AP}}-R_{\text{P}}}{R_{\text{P}}}, \quad (3)$$

$$R_{\text{AP}} = \frac{1}{G_{\text{AP}}},\ R_{\text{p}} = \frac{1}{G_{\text{p}}}, \quad (4)$$

we finally obtain:

$$\text{TMR} = \frac{2P_{\text{SF}}(P_1+P_3)}{1-P_{\text{SF}}(P_1+P_3)+P_1P_3}. \quad (5)$$

The derived formula demonstrates that when CVI possesses spin-filtering polarity opposite to the ferromagnetic electrodes (*i.e.*, $P_{\text{SF}} < 0$ while $P_1 > 0$ and $P_3 > 0$), the numerator of the expression is necessarily negative, whereas the denominator remains strictly positive. This condition inherently leads to a negative TMR value, which shows remarkable consistency with our experimental measurements.

When considering the antiparallel configuration where the ferromagnetic insulating layer is aligned parallel to one ferromagnetic electrode and antiparallel to the other, corresponding to stage III in Fig. 4b, the derived TMR expression takes the form:

$$\text{TMR} = \frac{2P_3(P_1+P_{\text{SF}})}{1-P_1P_{\text{SF}}-P_1P_3-P_{\text{SF}}P_3}. \quad (6)$$

The formula results indicate that when $P_{\text{SF}} < 0$, $P_1 > 0$, and $P_3 > 0$, TMR can potentially exhibit either positive or negative values. The negative TMR cases show perfect agreement with the results presented in Fig. 4b, whereas the positive TMR scenarios correspond to the coexisting positive and negative TMR phenomena observed in Fig. 4c. This comprehensive alignment between our theoretical predictions and experimental observations demonstrates strong reliability and robustly validates our proposed spin-filtering model.

Finally, bias-dependent TMR measurements were systematically performed on the FGT/CVI/FGT MTJ. First, the measurements at an increased bias of 200 mV (Fig. 5a and b) demonstrated that the device exhibited positive TMR throughout the 2–100 K temperature range, and the TMR value reached a minimum at 50 K, near the T_C of CVI, confirming that the influence of CVI remains significant even under higher bias conditions.

To directly observe the bias voltage dependence on the TMR sign, we conducted measurements at 2 K across varying bias voltages (Fig. 5c and d), which clearly showed TMR sign reversal from negative to positive with increasing bias. For deeper understanding of the origins of both bias voltage and magnetism of CVI on the TMR sign, we performed comprehensive *I*–*V* curve measurements under high and low resistance states at various temperatures and calculated the bias-dependent TMR at a temperature range of 2–80 K (Fig. 5e). These results enabled the construction of a detailed TMR contour plot as a function of both temperature and bias voltage (Fig. 5f).

The contour analysis reveals two distinct regimes: at low biases, TMR sign reversal occurs near the T_C of CVI (marked by the black dashed line), demonstrating the crucial role of the magnetic transition of CVI in driving temperature-dependent TMR sign reversal.

This supports our conclusion that the disappearance of the spin-filtering effect of CVI during its transition from ferromagnetic to an ordinary insulator causes the TMR sign reversal. Furthermore, our results reveal that below the T_C of CVI, bias-voltage-induced TMR sign reversal occurs, with the critical reversal voltage progressively increasing at higher temperatures (marked by the green dashed line). This bias-dependent TMR sign reversal phenomenon, extensively documented in previous studies, originates from localized states within the ferromagnetic electrodes.[21,23,36,37,57] Higher bias voltages enable greater participation of localized electrons in transport processes, thereby altering the effective spin polarization of both ferromagnetic electrodes. When the bias-induced polarization difference between electrodes outweighs the spin-filtering effect of CVI on TMR, bias-controlled sign reversal emerges. The temperature-dependent increase in critical reversal voltage likely reflects the need for stronger biases to overcome enhanced thermal disturbances to electron transport at elevated temperatures. Moreover, in Fig. 5f, two orange data points explicitly mark the experimentally observed positions with the coexistence of positive and negative TMR, based on which we deduce that the area enclosed by dashed lines represents the parameter space for potential TMR sign coexistence. This discovery opens new possibilities for designing multifunctional MTJ devices.

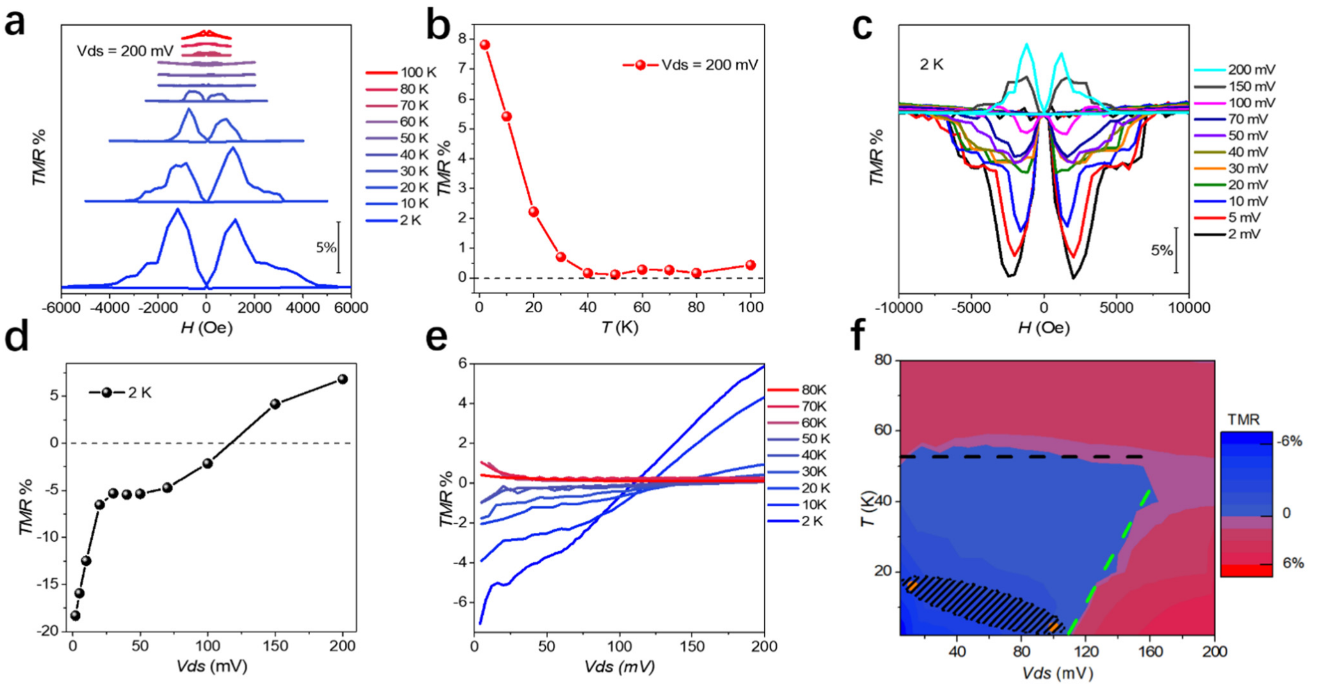

Fig. 5 Bias- and temperature-controlled TMR sign reversal of the FGT/CVI/FGT MTJ. (a) Temperature-dependent TMR curves of the CVI/FGT/FGT MTJ at a bias voltage of 200 mV. (b) Temperature dependence of the TMR peak value of the CVI/FGT/FGT MTJ at a bias voltage of 200 mV. (c) Bias-dependent TMR curves of the CVI/FGT/FGT MTJ at 2 K. (d) Bias dependence of the TMR peak value for the CVI/FGT/FGT MTJ at 2 K. (e) Bias-dependent TMR values of the FGT/CVI/FGT MTJ at different temperatures. (f) Contour plot of TMR as a function of temperature and bias voltage for the CVI/FGT/FGT MTJ.

Finally, it must be emphasized that both the theoretically predicted topological insulating properties of CVI and experimentally observed skyrmion configurations of CVI may exert significant influence on TMR characteristics. As is known, topological insulators possess insulating bulk states and topologically protected conductive surface states. Theoretical studies[58–60] have established that due to spin-momentum locking, unpolarized current passing through the topological surface states can generate net spin polarization. This spin-momentum locking has been detected *via* spin-resolved photoemission[61–63] and polarized optical spectroscopic techniques,[64] and the generation of spin-polarized currents in topological insulators has also been demonstrated in numerous transport experiments.[65,66] Thus, when CVI acts as a tunneling barrier, its potential topological boundary states can further regulate the spin-selective effect on electrons, thereby enhancing or suppressing TMR, or even reversing its sign.

In a recent study, Zadorozhnyi *et al.* theoretically demonstrated that spin filtering due to the skyrmion scattering can be more efficient by several orders of magnitude within certain electron concentration ranges than that of the ordinary ferromagnetic spin polarization.[67] Consequently, skyrmions present in CVI could further modulate spin selectivity, thereby influencing TMR performance. Furthermore, through a literature review, in MTJs with skyrmions, the TMR results usually do not display the double-plateau behavior of conventional MTJs but instead exhibit a continuously varying tunneling magnetoresistance process modulated by the size and density of skyrmions.[68–73] In our measurements of two FGT/CVI/FGT MTJs, we observed non-standard plateau regions with continuously varying tunneling magnetoresistance, as shown in stage II of Fig. 4b, suggesting the presence of non-negligible skyrmions in CVI.

In summary, our results demonstrate that while the TMR sign reversal in FGT/CVI/FGT MTJs is primarily governed by spin filtering in CVI, additional contributions from topological surface states and skyrmionic configurations may coexist. These potential secondary mechanisms warrant systematic investigation in future studies.

Conclusion

In conclusion, leveraging the topologically nontrivial ferromagnetic insulator CVI and the ferromagnetic metal FGT, we successfully fabricated CVI/FGT heterojunctions and FGT/CVI/FGT MTJs. Through Hall measurements conducted on the CVI/FGT heterojunctions, the incorporation of CVI resulted in a significant enhancement of the H_C of FGT. Specifically, at 60 K, which is close to the T_C of CVI, H_C is enhanced by 180%. This intriguing phenomenon is attributed to the AFM coupling that occurs between CVI and FGT. Subsequently, temperature-dependent sign reversal of TMR was observed through constant voltage tunneling measurements performed on the FGT/CVI/FGT MTJs. The TMR exhibited a negative value at lower temperatures, but as the temperature rose above 60 K, close to the T_C of CVI, the TMR transitioned to a positive value. The underlying mechanism for this sign reversal is believed to be the spin-filtering effect of CVI, which has an opposite polarity to the polarity of FGT. This discovery provides important experimental and theoretical foundations for future MTJ development by suggesting that the temperature of TMR sign reversal can be engineered through various approaches including the modulation of the T_C of CVI (*via* strain, gating, or other external stimuli) or the selection of magnetic insulator spacers with different T_C, potentially enabling room-temperature operation of this effect. Furthermore, we observed bias-dependent TMR sign reversal, as well as the coexistence of both positive and negative TMR signals under combined voltage and temperature modulation. This discovery suggests the potential for advancing conventional two-state MTJ operation to three-state functionality. This work significantly expands the design freedom for next-generation spintronic devices utilizing tunable TMR characteristics, paving the way for more efficient and versatile spintronic devices in the future.

Experimental methods

Crystal growth

CVI crystals were prepared *via* the chemical vapor transport (CVT) method. Cr powder (Alfa, 99.99%), V powder (Aladdin, 99.5%), and I beads (Aldrich, 99.999%) were vacuum-sealed (5×10^{-3} Pa) in an ampoule at an atomic ratio of 1 : 1 : 6. Subsequently, the temperature of the raw material end was set at 650 °C, while the crystal growth region at the other end was set at 550 °C. The growth process lasted for 8 days, followed by natural cooling. A large quantity of CVI crystals, each with a size of approximately 5 mm × 5 mm, were obtained in the crystal growth area.

Chemical composition characterization

The composition of the CVI crystals was characterized by field emission scanning electron microscopy (FE-SEM, JSM-7000F) and energy dispersive X-ray (EDX) analysis. A 15 kV acceleration potential was applied to the SEM. To determine the crystal composition, EDX analysis was performed on surface scans covering an area of 250 μm × 250 μm.

Device fabrication

The Ti (~3 nm)/Au (~7 nm) bottom electrodes were successfully pre-patterned *via* the standard ultraviolet lithography process. Subsequently, in a nitrogen-filled glove box, the FGT and CVI flakes were obtained through the mechanical exfoliation method. The optical microscopy (OM)-based method and atomic force microscopy were simultaneously used to determine the thickness of the FGT and CVI flakes (see Fig. S3). Then, the FGT and CVI flakes were transferred layer by layer onto the bottom electrodes *via* a transfer platform. The exfoliated flakes were stacked at random angles, thereby excluding the potential influence of the moiré superlattice. Due to material sensitivity, the devices were encapsulated with boron nitride (hBN) and the sealant (ELC-2500), (for the sealing performance of ELC-2500 on CVI see Fig. S11) followed by 120 °C annealing (10 min) to improve interfacial contact.

Magnetic transport measurements

All magnetic transport measurements were performed using the Physical Property Measurement System (PPMS-9T, Quantum Design). For CVI/FGT heterojunctions, we conducted transport and Hall measurements using the Resistivity Option with a constant current of 1 μA. For FGT/CVI/FGT MTJs, magnetic tunneling transport was characterized using the Electrical Transport Option with an applied voltage of 10–200 mV.

MOKE measurements

The Kerr signal was characterized using a MOKE measurement system (KMP-L, Truth Instruments). The MOKE measurements were performed using a normally incident HeNe laser beam (λ = 633 nm) with linear polarization and a focused spot diameter of approximately 5 μm. During the measurements, the magnetic field was consistently applied perpendicular to the in-plane direction of the device.

Author contributions

Q. Wang performed the experiments and wrote the manuscript. J. Liu performed the experiments and helped with data analysis. C. Yang, H. Zhao and F. Hou helped with data analysis. Y. Wu advised on the atomic force microscopy experiments. T. Min and T. Li conceived the idea and supervised the research.

Conflicts of interest

There are no conflicts to declare.

Note added after first publication

This article replaces the version published on 18 August 2025, which contained errors in the Abstract, Equation (4) and Conclusion.

Data availability

The data supporting this article have been included as part of the SI. Compositional characterization of CVI crystals; Optical microscopy images of the CVI/FGT heterojunction and pure FGT; Determination of the thicknesses for CVI and FGT; Temperature-dependent R_{xx} curve of CVI; Transport and anomalous Hall properties of the pure FGT; Enhancement of the H_C in another CVI/FGT heterojunction; Calculation results of charge transfer in the CVI/FGT heterojunction; Temperature-dependent HC curves of the FGT in a partially CVI-covered FGT heterojunction device; IV curve of FGT/CVI/FGT MTJ at 2 K; Temperature-dependent TMR sign reversal in another FGT/CVI/FGT MTJ; Salability verification of ELC-2500 UV-curable sealant on CVI thin layers. See DOI: **https://doi.org/10.1039/d5nr01813g**.

Acknowledgements

This work was financially supported by the National Key R&D Program of China (grant no. 2021YFA1202200).

References

1 N. Maciel, E. Marques, L. Naviner, Y. Zhou and H. Cai, *Sensors*, 2020, **20**, 121.

2 Y. Lv, R. P. Bloom and J. P. Wang, *IEEE Magn. Lett.*, 2019, **10**, 1–5.

3 V. K. Joshi, P. Barla, S. Bhat and B. K. Kaushik, *IEEE Access*, 2020, **8**, 194105–194146.

4 L. Zhang, J. Zhou, H. Li, L. Shen and Y. P. Feng, *Appl. Phys. Rev.*, 2021, **8**, 021308.

5 B. Chen, M. Zeng, K. H. Khoo, D. Das, X. Fong, S. Fukami, S. Li, W. Zhao, S. S. P. Parkin, S. N. Piramanayagam and S. T. Lim, *Mater. Today*, 2023, **70**, 193–217.

6 J.-G. Zhu and C. Park, *Mater. Today*, 2006, **9**, 36–45.

7 E. Y. Tsymbal, A. Sokolov, I. F. Sabirianov and B. Doudin, *Phys. Rev. Lett.*, 2003, **90**, 186602.

8 C. Tiusan, J. Faure-Vincent, C. Bellouard, M. Hehn, E. Jouguelet and A. Schuhl, *Phys. Rev. Lett.*, 2004, **93**, 106602.

9 I. J. Vera Marún, F. M. Postma, J. C. Lodder and R. Jansen, *Phys. Rev. B.*, 2007, **76**, 064426.

10 A. Kalitsov, P.-J. Zermatten, F. Bonell, G. Gaudin, S. Andrieu, C. Tiusan, M. Chshiev and J. P. Velev, *J. Phys.: Condens. Matter*, 2013, **25**, 496005.

11 T. Ma, Y. Zhu, P. A. Dainone, T. Chen, X. Devaux, C. Wan, S. Migot, G. Lengaigne, M. Vergnat, Y. Yan, X. Han and Y. Lu, *ACS Appl. Electron. Mater.*, 2023, **5**, 5954–5961.

12 F. Jin, J. Shao, Z. Zhang, W. Zhang, K. Liu, J. Li, K. Liu, K. Dai, Q. Wang, Q. Lv, E. Hua, P. Chen, Z. Huang, C. Ma, L. Wang, Y. Zhao and W. Wu, *Adv. Funct. Mater.*, 2023, **33**, 2303492.

13 R. Galceran, L. Balcells, C. Martinez-Boubeta, B. Bozzo, J. Cisneros-Fernández, M. de la Mata, C. Magén, J. Arbiol, J. Tornos, F. A. Cuellar, Z. Sefrioui, A. Cebollada, F. Golmar, L. E. Hueso, F. Casanova, J. Santamaría and B. Martinez, *Phys. Rev. B: Condens. Matter Mater. Phys.*, 2015, **92**, 094428.

14 M. A. Tanaka, T. Hori, K. Mibu, K. Kondou, T. Ono, S. Kasai, T. Asaka and J. Inoue, *J. Appl. Phys.*, 2011, **110**, 073905.

15 A. Thomas, D. Meyners, D. Ebke, N.-N. Liu, M. D. Sacher, J. Schmalhorst, G. Reiss, H. Ebert and A. Hütten, *Appl. Phys. Lett.*, 2006, **89**, 012502.

16 B. Huang, G. Clark, E. Navarro-Moratalla, D. R. Klein, R. Cheng, K. L. Seyler, D. Zhong, E. Schmidgall, M. A. McGuire, D. H. Cobden, W. Yao, D. Xiao, P. Jarillo-Herrero and X. Xu, *Nature*, 2017, **546**, 270–273.
17 C. Gong, L. Li, Z. Li, H. Ji, A. Stern, Y. Xia, T. Cao, W. Bao, C. Wang, Y. Wang, Z. Q. Qiu, R. J. Cava, S. G. Louie, J. Xia and X. Zhang, *Nature*, 2017, **546**, 265–269.
18 Z. Wang, D. Sapkota, T. Taniguchi, K. Watanabe, D. Mandrus and A. F. Morpurgo, *Nano Lett.*, 2018, **18**, 4303–4308.
19 W. Zhu, S. Xie, H. Lin, G. Zhang, H. Wu, T. Hu, Z. Wang, X. Zhang, J. Xu, Y. Wang, Y. Zheng, F. Yan, J. Zhang, L. Zhao, A. Patané, J. Zhang, H. Chang and K. Wang, *Chin. Phys. Lett.*, 2022, **39**, 128501.
20 W. Jin, G. Zhang, H. Wu, L. Yang, W. Zhang and H. Chang, *Nanoscale*, 2023, **15**, 5371–5378.
21 K.-H. Min, D. H. Lee, S.-J. Choi, I.-H. Lee, J. Seo, D. W. Kim, K.-T. Ko, K. Watanabe, T. Taniguchi, D. H. Ha, C. Kim, J. H. Shim, J. Eom, J. S. Kim and S. Jung, *Nat. Mater.*, 2022, **21**, 1144–1149.
22 Z.-A. Wang, X. Zhang, W. Zhu, F. Yan, P. Liu, Z. Yuan and K. Wang, *Chin. Phys. Lett.*, 2023, **40**, 077201.
23 W. Zhu, Y. Zhu, T. Zhou, X. Zhang, H. Lin, Q. Cui, F. Yan, Z. Wang, Y. Deng, H. Yang, L. Zhao, I. Žutić, K. D. Belashchenko and K. Wang, *Nat. Commun.*, 2023, **14**, 5371.
24 X. Zhang, B. Yang, X. Guo, X. Han and Y. Yan, *Nanoscale*, 2021, **13**, 19993–20001.
25 X. Guo, Y. Zhu, B. Yang, X. Zhang, X. Han and Y. Yan, *Appl. Phys. Lett.*, 2022, **121**, 042404.
26 H. Zhang, X. Man, Y. Zhang, W. Yang, P. Cui, X. Xu and Z. Zhang, *Phys. Rev. B*, 2024, **110**, 214424.
27 X. Li, C. Liu, Y. Zhang, S. Zhang, H. Zhang, Y. Zhang, W. Meng, D. Hou, T. Li, C. Kang, F. Huang, R. Cao, D. Hou, P. Cui, W. Zhang, T. Min, Q. Lu, X. Xu, Z. Sheng, B. Xiang and Z. Zhang, *Nat. Phys.*, 2024, **20**, 1145–1151.
28 S. Pan, Y. Bai, J. Tang, P. Wang, Y. You, G. Xu and F. Xu, *J. Alloys Compd.*, 2022, **908**, 164573.
29 S. Liu, X. Yuan, Y. Zou, Y. Sheng, C. Huang, E. Zhang, J. Ling, Y. Liu, W. Wang, C. Zhang, J. Zou, K. Wang and F. Xiu, *npj 2D Mater. Appl.*, 2017, **1**, 30.
30 L. Tang, Y. Zhou, C. Kang, B. Wen, J. Tian and W. Zhang, *Appl. Phys. Lett.*, 2024, **124**, 012403.
31 Y. He, S. Schneider, T. Helm, J. Gayles, D. Wolf, I. Soldatov, H. Borrmann, W. Schnelle, R. Schaefer, G. H. Fecher, B. Rellinghaus and C. Felser, *Acta Mater.*, 2022, **226**, 117619.
32 Z.-A. Wang, W. Xue, F. Yan, W. Zhu, Y. Liu, X. Zhang, Z. Wei, K. Chang, Z. Yuan and K. Wang, *Nano Lett.*, 2023, **23**, 710–717.
33 P. Chongthanaphisut, S.-K. Bac, S. Choi, K. J. Lee, J. Chang, S. Choi, S. Lee, M. Nnaji, X. Liu, M. Dobrowolska and J. K. Furdyna, *Sci. Rep.*, 2019, **9**, 4740.
34 P. Chongthanaphisut, K. J. Lee, S. Park, J. Jang, S. Lee, X. Liu, M. Dobrowolska and J. K. Furdyna, *J. Appl. Phys.*, 2020, **127**, 183902.
35 M. Julliere, *Phys. Lett. A*, 1975, **54**, 225–226.
36 W. Jin, G. Zhang, H. Wu, L. Yang, W. Zhang and H. Chang, *ACS Appl. Mater. Interfaces*, 2023, **15**, 36519–36526.
37 S. Zhu, H. Lin, W. Zhu, W. Li, J. Zhang and K. Wang, *Appl. Phys. Lett.*, 2024, **124**, 222401.
38 D. Kim, C. Kim, C.-O. Kim, S. S. Yoon, M. Naka, M. Tsunoda and M. Takahashi, *J. Magn. Magn. Mater.*, 2006, **304**, e356–e358.
39 L. V. Tho, C. G. Kim and C. O. Kim, *J. Appl. Phys.*, 2008, **103**, 07B906.
40 J. Kim, S. Son, M. J. Coak, I. Hwang, Y. Lee, K. Zhang and J.-G. Park, *J. Appl. Phys.*, 2020, **128**, 093901.
41 R. Obata, H. Sun, K. Samanta, N. A. Shahed, M. Kosugi, T. Kikkawa, A. Abdallah, K. Watanabe, T. Taniguchi, K. Suenaga, E. Saitoh, S. Maruyama, K. Hirakawa, K. D. Belashchenko, E. Y. Tsymbal and J. Haruyama, *Adv. Mater.*, 2025, **37**, 2411459.
42 C. Tan, J. Lee, S.-G. Jung, T. Park, S. Albarakati, J. Partridge, M. R. Field, D. G. McCulloch, L. Wang and C. Lee, *Nat. Commun.*, 2018, **9**, 1554.
43 S. Yuasa, T. Nagahama and Y. Suzuki, *Science*, 2002, **297**, 234–237.
44 J. M. George, L. G. Pereira, A. Barthélémy, F. Petroff, L. Steren, J. L. Duvail, A. Fert, R. Loloee, P. Holody and P. A. Schroeder, *Phys. Rev. Lett.*, 1994, **72**, 408–411.
45 C. Gould, C. Rüster, T. Jungwirth, E. Girgis, G. M. Schott, R. Giraud, K. Brunner, G. Schmidt and L. W. Molenkamp, *Phys. Rev. Lett.*, 2004, **93**, 117203.
46 A. V. Ramos, M.-J. Guittet, J.-B. Moussy, R. Mattana, C. Deranlot, F. Petroff and C. Gatel, *Appl. Phys. Lett.*, 2007, **91**, 122107.
47 J. S. Moodera, X. Hao, G. A. Gibson and R. Meservey, *Phys. Rev. Lett.*, 1988, **61**, 637–640.
48 M. Gajek, M. Bibes, A. Barthélémy, K. Bouzehouane, S. Fusil, M. Varela, J. Fontcuberta and A. Fert, *Phys. Rev. B: Condens. Matter Mater. Phys.*, 2005, **72**, 020406.
49 U. Lüders, M. Bibes, K. Bouzehouane, E. Jacquet, J.-P. Contour, S. Fusil, J.-F. Bobo, J. Fontcuberta, A. Barthélémy and A. Fert, *Appl. Phys. Lett.*, 2006, **88**, 082505.
50 M. Abbasi Eskandari, S. Ghotb and P. Fournier, *Phys. Rev. B*, 2024, **109**, 064405.
51 D. Jin, Y. Ren, Z.-z. Li, M.-w. Xiao, G. Jin and A. Hu, *Phys. Rev. B: Condens. Matter Mater. Phys.*, 2006, **73**, 012414.
52 Y. K. Takahashi, S. Kasai, T. Furubayashi, S. Mitani, K. Inomata and K. Hono, *Appl. Phys. Lett.*, 2010, **96**, 072512.
53 T. Song, X. Cai, M. W.-Y. Tu, X. Zhang, B. Huang, N. P. Wilson, K. L. Seyler, L. Zhu, T. Taniguchi, K. Watanabe, M. A. McGuire, D. H. Cobden, D. Xiao, W. Yao and X. Xu, *Science*, 2018, **360**, 1214–1218.
54 T. Song, M. W.-Y. Tu, C. Carnahan, X. Cai, T. Taniguchi, K. Watanabe, M. A. McGuire, D. H. Cobden, D. Xiao, W. Yao and X. Xu, *Nano Lett.*, 2019, **19**, 915–920.
55 K. Inomata, N. Ikeda, N. Tezuka, R. Goto, S. Sugimoto, M. Wojcik and E. Jedryka, *Sci. Technol. Adv. Mater.*, 2008, **9**, 014101.

56 J. S. Moodera, T. S. Santos and T. Nagahama, *J. Phys.: Condens. Matter*, 2007, **19**, 165202.

57 H. Pan, A. K. Singh, C. Zhang, X. Hu, J. Shi, L. An, N. Wang, R. Duan, Z. Liu, S. S. P. Parkin, P. Deb and W. Gao, *InfoMat*, 2024, **6**, e12504.

58 A. A. Burkov and D. G. Hawthorn, *Phys. Rev. Lett.*, 2010, **105**, 066802.

59 O. V. Yazyev, J. E. Moore and S. G. Louie, *Phys. Rev. Lett.*, 2010, **105**, 266806.

60 D. Culcer, E. H. Hwang, T. D. Stanescu and S. Das Sarma, *Phys. Rev. B: Condens. Matter Mater. Phys.*, 2010, **82**, 155457.

61 S. Souma, K. Kosaka, T. Sato, M. Komatsu, A. Takayama, T. Takahashi, M. Kriener, K. Segawa and Y. Ando, *Phys. Rev. Lett.*, 2011, **106**, 216803.

62 Z. H. Pan, E. Vescovo, A. V. Fedorov, D. Gardner, Y. S. Lee, S. Chu, G. D. Gu and T. Valla, *Phys. Rev. Lett.*, 2011, **106**, 257004.

63 D. Hsieh, Y. Xia, D. Qian, L. Wray, J. H. Dil, F. Meier, J. Osterwalder, L. Patthey, J. G. Checkelsky, N. P. Ong, A. V. Fedorov, H. Lin, A. Bansil, D. Grauer, Y. S. Hor, R. J. Cava and M. Z. Hasan, *Nature*, 2009, **460**, 1101–1105.

64 J. W. McIver, D. Hsieh, H. Steinberg, P. Jarillo-Herrero and N. Gedik, *Nat. Nanotechnol.*, 2012, **7**, 96–100.

65 C. H. Li, O. M. J. van't Erve, J. T. Robinson, Y. Liu, L. Li and B. T. Jonker, *Nat. Nanotechnol.*, 2014, **9**, 218–224.

66 C. H. Li, O. M. J. van't Erve, Y. Y. Li, L. Li and B. T. Jonker, *Sci. Rep.*, 2016, **6**, 29533.

67 A. Zadorozhnyi and Y. Dahnovsky, *J. Phys.: Condens. Matter*, 2020, **32**, 405803.

68 S. Chen, J. Lourembam, P. Ho, A. K. J. Toh, J. Huang, X. Chen, H. K. Tan, S. L. K. Yap, R. J. J. Lim, H. R. Tan, T. S. Suraj, M. I. Sim, Y. T. Toh, I. Lim, N. C. B. Lim, J. Zhou, H. J. Chung, S. T. Lim and A. Soumyanarayanan, *Nature*, 2024, **627**, 522–527.

69 Y. Guang, L. Zhang, J. Zhang, Y. Wang, Y. Zhao, R. Tomasello, S. Zhang, B. He, J. Li, Y. Liu, J. Feng, H. Wei, M. Carpentieri, Z. Hou, J. Liu, Y. Peng, Z. Zeng, G. Finocchio, X. Zhang, J. M. D. Coey, X. Han and G. Yu, *Adv. Electron. Mater.*, 2023, **9**, 2200570.

70 M. Zhao, A. Chen, P.-Y. Huang, C. Liu, L. Shen, J. Liu, L. Zhao, B. Fang, W.-C. Yue, D. Zheng, L. Wang, H. Bai, K. Shen, Y. Zhou, S. Wang, E. Liu, S. He, Y.-L. Wang, X. Zhang and W. Jiang, *npj Quantum Mater.*, 2024, **9**, 50.

71 S. Li, A. Du, Y. Wang, X. Wang, X. Zhang, H. Cheng, W. Cai, S. Lu, K. Cao, B. Pan, N. Lei, W. Kang, J. Liu, A. Fert, Z. Hou and W. Zhao, *Sci. Bull.*, 2022, **67**, 691–699.

72 B. He, Y. Hu, C. Zhao, J. Wei, J. Zhang, Y. Zhang, C. Cheng, J. Li, Z. Nie, Y. Luo, Y. Zhou, S. Zhang, Z. Zeng, Y. Peng, J. M. D. Coey, X. Han and G. Yu, *Adv. Electron. Mater.*, 2023, **9**, 2201240.

73 T. Xu, X.-Y. Guo, Y. Liu, H. Du and D.-F. Shao, *Adv. Funct. Mater.*, 2025, 2504100.